The Cryosphere Discuss., 6, 1963–2004, 2012
www.the-cryosphere-discuss.net/6/1963/2012/
doi:10.5194/tcd-6-1963-2012

The Cryosphere Discussions

Summer sea ice in the recent Arctic: morphological properties in the Pacific sector from the CHINARE 2010 cruise

H. Xie[1], R. Lei[2], C. Ke[3], H. Wang[4], Z. Li[5], J. Zhao[6], and S. F. Ackley[1]

[1]Laboratory for Remote Sensing and Geoinformatics, University of Texas at San Antonio, Texas, 78249, USA
[2]Key Laboratory for Polar Science of the State Oceanic Administration, Polar Research Institute of China, Shanghai, 200136, China
[3]School of Geographic & Oceanographic Sciences, Nanjing University, Nanjing, 210093, China
[4]Department of Earth Sciences, Zhejiang University, Hangzhou, 310027, China
[5]State Key Laboratory of Coastal and Offshore Engineering, Dalian University of Technology, Dalian, 116024, China
[6]College of Physical and Environmental Oceanography, Ocean University of China, Qindao, 266100, China

Received: 3 May 2012 – Accepted: 16 May 2012 – Published: 31 May 2012

Correspondence to: H. Xie (hongjie.xie@utsa.edu)

Published by Copernicus Publications on behalf of the European Geosciences Union.

Abstract

The Chinese National Arctic Research Expedition (CHINARE) in the summer 2010, primarily from 21 July to 28 August, in the ice zone of Arctic Pacific Sector, between 150° W to 180° W to 88.5° N, conducted comprehensive scientific studies on atmosphere-ice-ocean interactions, using icebreaker R.V. Xuelong. Measurements made included underway visual observations of snow and ice conditions at half-hourly time scale and EM31-measured ice thickness at one 12-day and eight short-term (3–4 h each) ice stations. The visual observation data are compared with AMSR-E ice concentration, ice thickness measured by a hanging EM31 from the vessel, and video-recorded image-derived ice concentration and pond coverage. A grid of 8 profiles of ice thickness measurements (four repeats) was conducted at the 12-day ice station (~ 86°50′ N–87°20′ N) in the central Arctic and an average 2 cm day^{-1} melt rate, primarily bottom melt, was found, after surface melting had almost ceased. The high bottom melt rate, as compared with previous results from other studies, is consistent with the high floe speed (mean 0.17 m s^{-1}) that is also larger than that previously reported. We also found that the daily AMSR-E ice concentration data can be used to map the marginal ice zone (MIZ) and its change. There are clear differences between the MIZ and pack ice zone in terms of ice concentration, thickness, ice type, floe size, as well as pond coverage. Results indicate that, as compared with the 2005 data from the Healy/Oden Trans-Arctic Expedition for the Arctic Pacific Sector (9 August to 10 September), the 2010 was first-year ice dominant (vs. the multiyear ice dominant in 2005), 70 % or less in ice concentration (vs. 90 % in 2005), 94–114 cm in ice thickness (vs. 150 cm in 2005). No snow cover was observed on the ice south of 78° N and 8–10 cm mean snow depth due to new snowfall events, which melted away after 17 August (vs. no snow cover south of 84.3° N or ~ 10 cm snow depth further north in 2005). Those changes indicate the continuation of ice thinning, less concentration, and younger ice after the 2007 shift, when a record minimum sea ice extent was observed. Overall, the measurements provided a valuable dataset of sea

TCD
6, 1963–2004, 2012

ice morphological properties over the Arctic Pacific Sector in summer 2010, which confirms, by comparison with previous data, that a "new normal" of Arctic sea ice is now present and is a benchmark for measurements of possible future changes.

1 Introduction

The Arctic sea ice has been observed shrinking and thinning during the past three decades (Serreze et al., 2007; Stroeve et al., 2007; Comiso et al., 2008; Perovich, 2011). Its first year ice (FYI) has replaced much of the multiyear ice (MYI) (Kwok and Rothrock, 2009; Maslanik et al., 2007; Nghiem et al., 2007). The more than 11 % per decade (in recent 3 decades) in decline in September ice extent (Perovich, 2011) is far larger than the prediction of modeling results (IPCC-AR4). September 2007 was the record low ice extent since satellite records, with September 2011 as the second lowest (NSIDC). The five years from 2007 to 2011 have been the five lowest years in summer sea ice extent, recently described as the "new normal" condition of Arctic summer sea ice (2011 Arctic Report Card). The most significant decline of ice extent (2007–2011) was between 150° W and 120° E (including the Chukchi and East Siberian Seas) as compared with the September median ice extent from 1979 to 2000. In particular, the Pacific sector between 150° W and 180° W saw very significant decline in 2007, recovered somewhat in 2008, and has since maintained similar minimum extents in 2009, 2010, and 2011. From spaceborne measurements, ice concentration decreased from primarily 90 % over the central Arctic in the 1978–2000 period to less than half of the region at 90 % in the 2003–2008 period (Kwok and Rothrock, 2009). Ice thickness is technically more difficult to measure from space. However, the combined submarine and ICESat records show that the average ice thickness of the central Arctic in fall has decreased from 3.0 m (1958–1976) to 1.4 m (2003–2007) (Kwok and Rothrock, 2009). The decommissioning of ICESat in 2009, coupled with the delayed launch of ICESat2 in 2016, suggests there will be a significant gap in the high resolution ice thickness record. The launch of CryoSat in April 2010 may provide significant altimetric data to

TCD
6, 1963–2004, 2012

fill the gap. However, the different resolution scales of ICESat's laser altimeter (70 m) compared to CryoSat's radar altimeter (250 m) may make large scale thickness change difficult to compare between the two systems. The CryoSat radar altimeter also bases its ice thickness estimation on assumed penetration of the snow cover to the ice surface to measure ice elevation, while the ICESat laser altimeter reflects from and measures the upper snow surface elevation (Zwally et al., 2002, 2008; Giles et al., 2007, 2008; Xie et al., 2011). During Arctic summer however, the ice/snow surface is rather wet, characterized by numerous and spatially extensive melt ponds (Lu et al., 2010; Perovich, et al., 2007, 2009; Eicken et al., 2004). This wet ice/snow surface will likely cause large errors to the CryoSat estimates of ice thickness since the summer and winter behavior of the snow cover is radically different at CryoSat's radar wavelengths (Haas and Druckenmiller, 2009). Therefore, while extremely important, the accuracy of CryoSat data for summer sea ice thickness estimation may be problematic. Ship-based and airborne observations provide some alternative methods to discern regional-scale changes in ice thickness in summer seasons from 2009 and assist CryoSat validation until 2016 when ICESat-2 data are planned to become available.

The Chinese National Arctic Research Expedition (CHINARE) from 1 July to 20 September 2010, conducted comprehensive scientific studies on atmosphere-ice-ocean interactions and the marine ecosystem's response to climatic change in the Arctic Pacific Sector, using icebreaker R.V. Xuelong. Among a team of 50 scientists, the sea ice team of 10 collected a comprehensive data set on the sea ice morphological and physical properties of the sector, in particular between 150° W to 180° W up to 88.5° N, and from 21 July to 28 August.

This paper presents our results based primarily on (1) underway visual observations of sea ice at half-hourly intervals and automatic video-camera recording of sea ice at a 10-s interval and (2) on-ice measurements of snow and ice thickness using an electromagnetic induction instrument, the Geonics EM31 (9.8 kHz), at one 12-day and eight short-term (3–4 h each) ice stations. The visual observed ice thicknesses are also compared with those from the hanging EM31 on the left side of the ship at a height of

TCD
6, 1963–2004, 2012

3.5 m above waterline and 6 m from the ship, at a rate of one reading per second (Wang et al., 2012). The visual observed ice concentrations are also compared with the corresponding AMSR-E ice concentrations. The implication of AMSR-E ice concentration data for mapping the Arctic marginal ice zone is further discussed. A previous comparison for the Arctic Pacific Sector between the HOTRAX05 (Healy/Oden Trans-Arctic Expedition 2005) and the AOS94 (Arctic Ocean Section 1994) expeditions showed overall reduced ice concentration for the 70–80 ° N latitudes and increased pond coverage for the 75–80° N latitudes, while the ice concentration and pond coverage did not show much change for other latitude degrees (above 80° N (concentration and pond coverage) and below 75° N for pond coverage) (Perovich et al., 2009). Results from this 2010 cruise are compared with the HOTRAX05 to extend this comparison into the regime shift period, post 2007, that has been characterized through satellite imagery analysis as the "new normal" period for Arctic summer sea ice.

2 Study area and methods

Figure 1 shows the cruise track and ship-based observations of sea ice and ice stations, primarily in the Chukchi Sea, Beaufort Sea, and Central Arctic Ocean. The underway ship-based ice observations are divided into 3 legs, the westward, northward, and southward legs. The observation team of 10 persons (4-h shifts) during the cruise was arranged to observe the sea ice situation from the ship's bridge, on a half-hourly observation interval schedule. The observation protocol, similar to the Antarctic Sea ice Processes and Climate (ASPeCt) protocol (Worby and Allison, 1999; Worby et al., 2008), records all the information related to ice concentration, floe size, ice type, melt pond coverage, and ice and snow thickness. For multiple ice type situations, ice type, floe size, concentration, and thickness are recorded separately for each ice type. A ball of 30 cm in diameter mounted on the port side (4 m above waterline) was used as a reference to visually estimate ice thickness of overturning ice blocks adjacent to the ship's hull. The ship's length (167 m) and width (22.6 m) were used as references to estimate

TCD
6, 1963–2004, 2012

the floe size. Sediment laden ice, biological richness, and regular weather conditions were also recorded as commentary remarks. The combined information from all these data provides a broad view of the sea ice cover for its spatial and temporal variations over the Arctic Pacific Ocean for the study period. Visual observations of ice concentration are compared with the AMSR-E ice concentration, 12.5 km in cell size from the National Snow and Ice Data Center (NSIDC), for validation purposes in this paper.

In support of human observations of sea ice conditions, two independent video/digital camera systems were deployed as part of the underway observations of sea ice during the cruise. The camera systems were mounted on both port and starboard sides of the ship's bridge, at a height of 26 m above waterline, to record oblique-view images of the ice field either at a capture rate of one image per 10 s (EISCam, Weissling et al., 2009) or per 1 min. This paper only shows the results from the EISCam system. The EISCam capture rate was chosen to provide image overlap of ~ 20 % at the ship's average speed through the ice. The primary purpose of the video camera system was to support the visual observations of sea ice at a significantly higher sampling rate (half-hour vs 10 s), thus providing a means to error check the human observations as well as to serve as quality control for inevitable visual bias among observers, perhaps due to varying experience and training. The design of the EISCam system also allows for true-scale orthorectification of individual still images from the video recording, based on the image, lens, and camera geometry, using an automated IDL (Interactive Data Language)-based processing code to process the imagery, including production of basic statistics (Weissling et al., 2009). Individual orthorectified images from EISCam can then be analyzed individually or mosaiced for ice type classification, ice concentration, melt-pond size and areal coverage, floe size, and lead width (Weissling et al., 2009). In this paper, the EISCam derived ice concentration and melt pond coverage are also compared with visually observed ice concentration and melt pond coverage.

One 12-day and eight short term (3–4 h each) ice stations (Fig. 1b) were conducted during the cruise, with detailed snow, ice, and pond physical properties measured and sampled. The first ice station (IS1-0727) was in the Chukchi Sea, near Barrow, Alaska

TCD
6, 1963–2004, 2012

on 27 July. The last one (IS8-0824) was in the Beaufort Sea on 24 August. The 12-day ice station (~ 86°50′ N–87°20′ N) was in the Central Arctic Ocean from 7–19 August. Representative photos of typical snow and ice sampled at each station and on ship are shown in Fig. 2. A Geonics EM-31 electromagnetic induction sensor was used for snow and ice thickness measurements along designed profiles in each ice station. It was hand carried by the same operator at a relatively fixed position above the surface (instrument height ~ 0.845 m) collecting data (discrete sampling) in vertical dipole mode (see photo IS3 of Fig. 2). At each sampling point, in order to compensate for the thickness heterogeneity of sea ice in different directions, two data samples were recorded, one with the instrument's longitudinal direction parallel to the walk direction and the other with the instrument's longitudinal direction perpendicular to the walk direction. The mean of the two readings at one point is counted as one discrete sample reading. The EM-estimated thicknesses were compared with borehole-drilling thicknesses with good agreement (3–7 % error, not shown). At each short-term ice station, one or more profiles were surveyed with a fixed sampling interval of approximately one meter or in a continuous mode at a rate of one reading per second. In the 12-day ice station, a grid of 8 profiles of 100 m in work zone 2 and two other profiles (200 m and 125 m) in work zone 3 were surveyed with repeat intervals of 3 or 4 days. A total of 31 profiles and 2957 sampling points were performed in the 8 short-term and one 12-day ice stations (Table 1).

3 Results

During the over two-month cruise, the ice was first seen at 69.80° N/168.97° W, at 20:55 UTC, 21 July, just north of the Bering Strait in the Chukchi Sea. This ice was part of an ice strip, less than 100 km in width (east-west) and 200 km in length (north-south), as a tongue that extended out from the main pack ice to the north. The ice was last seen at 75.61° N/172.16° W, at 12:15 UTC, 28 August (Fig. 1). It therefore retreated about 650 km over the 38-day period from 21 July to 28 August. Overall, during

TCD
6, 1963–2004, 2012

the entire period, ice was in a stage of rapid melting and retreating, but some precipitation events modified the melting, with at least two moderate snowfall events from 31 July to 4 August, two additional small snowfall events from 7–11 August, one rainfall event on 17 August, and several rainfall events from 26–28 August. With a few exceptions, the air and water temperatures were generally larger than 0 °C south of the 74.5° N (prior to 29 July), while closer to or lower than 0 °C north of the 75° N (Fig. 3). All the snowfall events occurred when the air temperature was close to or below −2 °C. Obvious freezeup was seen on 24 August (Fig. 2) when air temperature was below −2 °C between 82–81 ° N during the southward leg (Fig. 3). Water temperature north of 75° N was generally between 0 to −1.5 °C, which was not low enough for sea water to freezeup. Therefore, the freezeup mostly occurred due to the fresher melt water inside the melt ponds during the cruise period. Freezeup over the melt ponds was observed at ice stations, especially at high latitudes. The rainfall event during the 12-day ice station (northward leg) was related to the warm spike (at 87.2–87.3° N) up to 1.9 °C on 17 August (Fig. 3), which resulted in a distinct snowmelt over ice surface and a decrease in surface albeo (Lei et al., 2012). During the entire period over the ice zone, weather most of the time was foggy and/or overcast sky, with only a few sunny and scattered cloudy sky conditions. It was interesting that the weather was overall clearer during the local night time (still no darkness though) than local day time.

3.1 Visual observations of snow and ice properties

As shown in Fig. 1, the westward leg was a short one (~ 280 km) and was entirely within the marginal ice zone (MIZ) less than 50 km south to the ice edge from 24 July, 10:00 UTC to 25 July, 06:30 UTC. Ship speed was 6–8 kts. Salinity of the surface water (based on measurements by an underway continuous flow system of R/V Xuelong) along this leg was about 26 psu, less than the 31–34 psu measured in open water without ice present before entering the MIZ. This indicates the sea ice was in the melting process which reduced the salinity of sea water at the surface. Ice concentration (IC) in the first half of the leg was 40 % or less, then increased to 60–90 %, and decreased

TCD
6, 1963–2004, 2012

again in the last 40 km before exiting the ice zone (Fig. 4d). With a few exceptions, AMSR-E ice concentration was generally in good agreement with visual observed ice concentration (Fig. 4d). Floe size was less than 20 m for the first half of the leg, increased to between 20–100 m, and to 100–500 m, and again to less than 20 m in the last 40 km before exiting the ice zone (Fig. 4d), a similar pattern as observed for the ice concentration. Ice thickness was between 40 to 150 cm; a loose surface layer of granular decomposing sea ice (Perovich et al., 2002, 2003), which can be easily mislabeled as a snow layer, was less than 10 cm (not shown); and melt pond coverage (MC, i.e., pond-covered ice) was between 0 to 30 % of ice with a mean of 10 %. Ice type was primarily first year ice, level ice dominant, with ridged area between 5–10 % of the ice area. Some small isolated floebergs (20–40 m), with 2–5 m elevation above sea level, were also seen. These should be pieces of highly ridged, perhaps multiyear ice. Besides those clean/white ice types, there was an ice type of dirty ice (brownish, many holes inside, large roughness) (Fig. 2a). Dirty ice could have been formed due to sediment entrainment near coast regions, either from anchor ice origin or suspension freezing origin (Darby et al., 2011; Eicken et al., 2005; Kempema et al., 1989). Fraction of dirty ice ranged from 1–5 % in the central sector of the leg and 10–15 % (can be up to 70–80 %) near ice edges of the leg. Many seals (less than 10 together) and walruses (herds of tens to hundreds) were seen closely associated with dirty ice. Before the ship entered this MIZ westward, the ship went northward and traveled partially through the east part of an ice strip, from 03:00–06:30 UTC, 24 July, where the same type of dirty ice as seen in the westward leg, associated with many seals and walruses, and one polar bear, the only one seen in the entire cruise. This ice strip was in the same ice strip first seen on 21 July (the southernmost portion of the strip) and the ship traveled 2 h northward before it left the strip. The ship was then hit by a big wind storm from late 22 July to 23 July and was forced to park near the Alaska coast for a day before it came back to enter the ice strip again on 24 July.

The northward leg started near Barrow, Alaska at 71°21.23′ N/156°56.66′ W, 25 July, and ended at 88°21.33′ N/177°31.12′ W, 20 August. One 12-day and six short-term (3–

TCD
6, 1963–2004, 2012

4 h each) ice stations were conducted on the northward leg. The southward leg started 20 August and ended (out from the ice zone) at 75°30.6′ N/172°9.6′ W, 28 August. Two short-term ice stations were conducted on this leg. The ice observation results are included in Fig. 4a–c.

The Marginal Ice Zone (MIZ) is defined as the ice area where open ocean processes (mostly waves and swells) change significantly the dynamical properties of the sea ice cover, usually as a distinguishable difference in floe size and ice concentration from the pack ice zone (Squire, 2007; Leppäranta, 2005). Based on Fig. 4a, the region south of 75° N for the northward leg and south of 80° N for the southward leg can be defined as MIZ in this study. The clear boundary between the MIZ and pack ice zone is where the ice concentration immediately drops below 60 % in the MIZ. In the MIZ, ice concentration was highly variable from 0 to 90 % with a mean of 30 % (from a total 88 observations in the northward leg and 66 in the southward leg). In the pack ice zone, the concentration was overall larger than 50 %, with a mean of 66 % (272 observations) for the northward leg and 71 % (179 observations) for the southward leg.

In comparing visually observed ice concentration and AMSR-E ice concentration for the northward and southward legs (Fig. 4a), the overall patterns from the two datasets match well, although the AMSR-E ice concentration is overall higher (lower) than visually observed in the pack ice zone (MIZ). The latitudinal extents of MIZ, however, from both datasets were clearly mapped and were quite the same: 71.5–75° N (~ 350 km) for the northward leg (from 25–30 July) and 75.5–80° N (~ 450 km) for the southward leg (from 25–28 August). (Note that the northward limit of the MIZ at the end of July (75° N) corresponds to the ice edge (75.5° N) in the last part of August). This suggests that daily AMSR-E ice concentration data can be used to map the MIZ and its change.

Melt pond coverage (MC) varied differently in the MIZ and the pack ice zone, with overall similarities in the two legs, and within the two zones (Fig. 4a). First, the MC was overall lower in the MIZ than in the pack ice zone, i.e., 16 % vs 23 % for the northward leg and 10 % vs 33 % for the southward leg; second, in the pack ice zone, the MC shows an overall decreasing trend northward (i.e., from low latitude to high latitude),

TCD
6, 1963–2004, 2012

and it is even more obvious in the southward leg. The MC was up to 70 % around 81° N (southward leg), on late 24 August, where dominant ice (80 % of the ice) had thickness from 50–80 cm, melt ponds were in a status of almost bottom melt through or already bottom melted (Fig. 2b), which left many new thin (10–30 cm) ice lenses (formed on the surface of refrozen melt ponds) floating everywhere. This new ice (primarily from freshwater of melt ponds) can be easily confused as new sea ice (saltwater ice). The other ~20 % of the ice here, about 1.5 m in thickness, was still thick old ice, with ridged area of 30 % and blue color ponds, indicating blue ice below (second year or multi-year ice) (Fig. 2b).

Ice thickness and floe size also show obvious differences between the MIZ and in the pack ice zone (Fig. 4b, c1, c2). In the MIZ, ice thickness of the dominant ice type (highest concentration) was ~ 100 cm in late July (northward leg) and thinned to less than 50 cm in late August (southward leg), while floe size was typically 2 to 100 m. In the pack ice zone, floe size of dominant ice type was between 500 m to 10 km; ice thickness shows an overall latitudinal trend of increase moving northward (northward leg), or decrease moving southward (southward leg); the decreasing is more dramatic in the southward leg (Fig. 4c2), indicating melting has broadly occurred as of late August. Figure 4e shows the distribution and basic statistics of the ice thickness (from Fig. 4c1, c2). For the northward leg, majority of ice thicknesses were between 100 to 150 cm, with mean 114 ± 39 cm and median 120 cm for the entire leg, and mean 119 ± 37 cm and median 120 cm for the pack ice zone alone (not shown). For the southward leg, it shows two peak thicknesses: 20–30 cm, mostly in the MIZ where significant melt occurred into late August, and 130–150 cm, mostly in the high latitude area, with mean 94 ± 52 cm and median 100 cm for the entire leg, and mean 120 ± 38 cm and median 130 cm for the pack ice zone alone (not shown). None of these two thickness distributions (northward and southward) shows a single peak with long tail to right, which is a common ice thickness distribution from other means such as field measurements and remote sensing (Xie et al., 2011; Zwally et al., 2008; Weissling et al., 2011; Haas et al., 2008). This indicates that the visual observation of ice thickness (even at the half hourly rate

TCD
6, 1963–2004, 2012

in this cruise) is still very selective of the level ice thickness and probably very much undersampled.

Figure 4c also shows the snow and ice thickness (green plus) from the hanging EM-31 measurements (Wang et al., 2012) for comparison purposes. The EM31 thickness is at one per one second of latitude (or one per every ~ 30 m in distance) averaged from the original one reading per one second (in time). Averaging in this way can remove variations in sea ice due to differences in ship speed (a couple of kts to 12 kts). The distributions of the EM31 thickness data are shown in Fig. 4f, with dominant peak in the lower thickness (80 cm and 60 cm respectively for the northward and southward legs) and long tail to the right (maximum thickness 494 cm and 488 cm respectively for the northward and southward legs). This is the common type of sea ice thickness distributions and indicates the reasonable EM31 sampling and representative measurements of ice thickness. The EM31 thickness is a combined snow and ice thickness; as indicated before, there were about 10 cm new snow cover over the ice from the 79.5–87° N where EM31 had data (Fig. 4c1); those new snow melted away however by the end of the 12-day ice station. The thinner dominant ice thickness, 10 cm (or more) less than before, is clearly seen from the 87.5° N northward (i.e., after the 12-day ice station) (Fig. 4c1). The second EM31 thickness mode of the northward leg was 180 cm (the ~ 10 cm new snow depth included), which is larger than the visual-observed ice thickness mode 150 cm (Fig. 4g) for the same period where both EM31 and visual observation had data. If not including the 10 cm of new snow depth, the difference between the two modes is only about 20 cm. This indicates that the visual observations may be selectively ignoring the dominant peak (lower peak) but catching well the second peak (higher peak). From Fig. 4c1, it is clear that the visual-observed thickness is above the dominant peak (70–80 cm), except a few open water records (0 ice thickness), and below the second peak (180 cm), with much sparser sampling, i.e., 184 (visual) vs 23,524 (EM-31).

For the southward leg, the EM31 thickness had only one peak, 60 cm, which is less than the dominant peak 80 cm of the northward leg. One reason is that the 10 cm new

TCD
6, 1963–2004, 2012

snow seen in the northward leg did not exist in the southward leg; the other reason was the overall bottom melting seen in the 12-day ice station (total ~ 20 cm) should have occurred everywhere during the southward leg period. It is also of interest to see the EM31 thickness showed two different patterns in the southward leg, separating around 83.5° N (Fig. 4c2). Southward to 83.5° N, similar thickness structure was seen as in the northward leg: a dominant peak (60 cm) at the lowest thickness, a second peak (~ 170 cm) in the top thickness, with visual-observed ice thickness in between. Continuing southward, south of 83.5° N, the EM31 thickness structure has the 60 cm peak only, with a slight variation between 81.5–80.5° N, where the dominant ice thickness is ~ 100 cm. This was the section with the highest melt pond coverage (up to 70 % around 81° N, A2), with dominant ice thickness 50–80 cm from visual observations. In the marginal ice zone, the dominant 60 cm was overall larger than the visual-observed ice thickness (less than 50 cm). Overall, visual observation however is much undersampled as compared with the EM31, i.e., 230 (visual) vs. 36 401 (EM31) for the southward leg.

The EM31 provides detailed information on ice thickness and its change along the ship track. Maximum ice thickness from EM31 was over 4 m. Note that the hanging EM31 (3.6 m above waterline) was struck three times by isolated thick floebergs during the entire cruise (Fig. 2c shows a floeberg 10 m in diameter and over 4 m above the sea surface on 26 August that was struck by the hanging EM31). Both visual observations and hanging EM31 provide significant and independent measurements of ice physical properties, and are equally important and needed. Particularly, the high density of sampling ice thickness (once per second) from the hanging EM31 is invaluable and should be performed for any and each ship opportunity to the polar regions, particularly with the current lack of satellite lidar with the demise of ICESat.

3.2 EISCam for capturing detailed ice conditions

EISCam video images (one per 10 s) were processed and orthorectified. Fractional sea ice, melt pond, and lead (open water) were then extracted from each individual

TCD
6, 1963–2004, 2012

orthorectfied image using a band threshold classification approach described in Weissling et al. (2009). Figure 5 shows an example of the processing and threshold classification results. The threshold values for classes should be changed depending on the weather condition of image acquisition. Fractions of sea ice and melt ponds are aggregated into ice concentration (IC), and then melt pond coverage (MC) is derived using the fraction of melt pond over ice concentration. For the Fig. 5 case, the IC and MC are respectively 91 % and 30 %. Figure 6 is an example showing the time series of video image-derived IC and MC from 21–24 August (first half of the southward leg). The image-derived IC and MC (not shown) in 10 s time scale provide detailed information while with high variability, which might not be suitable or needed for large scale analysis. The 30 min moving-average IC and MC give better representation of ice and pond conditions with less variability than the 10 s time scale. Ship-based visual observed IC was overall smaller than the EISCam IC before 23 August while it matched reasonably well from 23–24 August, with an overall mean 71 % from visual observations for the 21–24 August period, which is less than the 84 % from EIScam for the same period (Fig. 6).

EISCam MC (Fig. 6) was overall larger from 21 August to the middle of 22 August than those from the middle of 22 August to the middle of 24 August, with a slight increasing trend for the late period (middle of 22 August to the middle of 24 August). Ship-based visually observed-MC from 21–24 August, however, was overall flat in the beginning and slightly increased trend late (Fig. 4a2), with an overall mean 32 %, much larger than the 14 % from the EISCam for the same period from 21–24 August. We note: (1) the big differences in sampling (10 s vs 30 min) and (2) totally different area of sampling (left-side looking 28 – 104 × 109 m, i.e., Fig. 5, vs a circle of 1 km radius). While the MC percentage probably did not change within these ranges, the larger area (1 km circle) can distort an observation of this type, since it is an oblique view leading to an area overestimate by an observer for distant ponds (Weissling et al., 2009). This might explain the overall larger mean from visual observed-MC than that from the EISCam-derived MC. Overall, the EISCam system provides an automated approach to collect

TCD
6, 1963–2004, 2012

sea ice conditions and then extract useful information such as ice concentration, pond coverage in great detail. It is also a permanent record that can be reanalyzed, unlike a visual observation that disappears as fast as it is made. EISCam data can also be used to derive spatial distributions of melt pond size, floe size, and lead width.

3.3 Ice thickness distribution from the eight short-term ice stations

Figure 7 shows the snow and ice thickness distribution and basic statistics measured by EM31 from the 8 short-term ice stations. The IS1 and IS2 show the highest mean, median, and mode ice thickness. The IS1 was in the MIZ (see Fig. 4a1) with overall thicker first year ice or second-/multi-year ice, while the floe size is 100 m or less. The ice floe of IS2 was just off the Xuelong, the only ice station that scientists and instruments were dropped down by a hanging cart from the ship (see a photo in Fig. 2). The measured ice thickness for this floe might have been contaminated by small floes submerged under the measured floe when Xuelong broke through the ice and parked on or next to the floe. IS3-5 were all conducted after or with two snowfall events occurred in the area, adding ~ 6 cm new snow to IS3, and ~ 8 cm to IS4 and IS5. Walking with the carried EM31 on such new/loose snow surface, it is easy to step into snow about 6–9 cm, or average of 8 cm that is used in this study to correct the instrument height above the snow surface to derive the true snow and ice thickness. IS5 was an ice floe over 300 m, and some measurements conducted over ice ridges show up to 5 m in thickness. IS6 (20 August) was the northernmost station conducted in the cruise and was just one day after the 12-day station (7–19 August) and 3 days after a slight rainfall event (on 17 August), which caused new snow to completely melt away from the previous granular top surface of the ice, a firn surface showing almost no steps into it, with mean depth ~ 0.1 m (granular decomposing sea ice) and mean ice thickness below that of ~ 1.53 m. Both IS7 and IS8 were conducted during the southward leg, both showing a two-peak thickness distribution, with granular decomposing ice on surface with mean depth of 0.1 m. The thinner peak (1.2 m for the IS7 and 1.0 m for IS8)

TCD
6, 1963–2004, 2012

is overall flat ice and/or ice closer to melt ponds, while the thicker peak (2.0 for IS7 and 1.4 m for IS8) is overall ridged ice.

3.4 Ice thickness distribution and change from the 12-day ice station

The 12-day ice station from 7–9 August as shown in Fig. 8 was on a more than 10 km by 10 km floe, mostly thick first-year ice (Lei et al., 2012), with average melt pond coverage of 30 % of ice and mean ice thickness of around 1.8 m. EM31 measurements were performed in work zone 2 (four repeats) and zone 3 (three repeats). Different settings were used for the EM31 measurements, a grid of 8 profiles (100 m long and 10 m apart) for zone 2 and two perpendicular profiles (200 m for P1 and 125 m for P2) for zone 3 (Fig. 8a, b). Due to the snowfall events before 7 August, plus two more small snowfalls on 7 and 11 August, the new snow cover of 0.06–0.10 m was not melted until starting on 17 August when a one-hour rainfall event started to melt the new snow away. The 18th and 19th were overall sunny, the best days during the 12-day station. Snow on ice of melt ponds was completely melted away and became water on thin ice of the ponds or water only without ice in some local areas of ponds. So only the last measurements conducted on 18 or 19 August included some surface melting, besides bottom melting, which was the dominant melting process in the 12-day station period. Before 17 August, the area might have had some surface gains due to the two small snowfall events. Figure 8c shows the overall thinning from a mean 1.89 m (10 August) to 1.71 m (19 August) in the work zone 2, and from 1.76 m (11 August) to 1.60 m (18 August) in the work zone 3, i.e., a mean thinning of about 2 cm day^{-1} for zone 2 and 2.5 cm day^{-1} for zone 3.

Figure 9 shows examples of thickness measurements and changes for work zone 2 (four repeats) and zone 3 (three repeats). It is clear that the sea ice thickness varied a lot, i.e., thicker closer to ridges (the locations at 100 m of A and 0 m of C) and thinner closer to large melt ponds (the location at 160 m of C) or open leads (the location at 82 m of B). Those locations also refer to Fig. 8. All other small valleys in the profiles were associated with small melt ponds nearby. This indicates that melt ponds (and

TCD
6, 1963–2004, 2012

open leads) not only can accelerate the surface melting but also accelerate the melting in the bottom or nearby of ponds and leads, since more solar radiation penetrated through the water and/or thinner ice can be used for bottom melting under or nearby the ponds and leads. There is also general bottom melting due to heated (or warmer) ocean water underneath moving forced by ocean currents. This is seen as consistent and general thinning everywhere along each profile. The thickness differences between the last two measurements for all profiles are always slightly larger than the differences between any two earlier measurements for the same profile. This is consistent with our observations mentioned earlier that there was some surface melting on the 18th and 19th due to a rainfall event on the 17th and overall larger than 0 air temperature on the 1th and 18th.

The point measurements of snow and ice thickness based on the EM31 over the 8-profile grid in one day (one repeat) can be used to produce a thickness map showing the spatial distribution of the thickness (as shown in Fig. 10). Geostatistical approach, here the ordinary Kriging method, is used to produce the thickness map. The Fig. 10 clearly shows the spatial thickness distribution for the first (A) and last (B) repeats, and the difference map (C) of the two repeats. The thicker ice was in the upper left corner (ridge) and lower right portion of the area (no melt ponds), while the thinner ice were primarily in upper right (next to large open leads) and lower left (multiple melt ponds) portions of the area. The largest thickness changes (melt) occurred: (1) along the top edge (ridge on the top left and open leads on the top right) and (2) new opening crack along or crossing the profile 5 (clearly seen in the Fig. 8b). The opening crack was narrower than 20 cm and almost covered by new snow (higher albedo) in the first 5 days, and gradually widened to 50 cm or more in some local portions by the end of the station period. The opening crack introduced more solar radiation to melt the ice (both lateral and bottom melts), which is clearly seen in this case. It is also clear that, even along the opening crack from top edge to bottom edge of the Fig. 10, the melt rate was quite different. The melt rate seems lower in the top half (not including the very top part where it is very close to the wide open water) than in the bottom half, while the

TCD
6, 1963–2004, 2012

general thickness in the top half seems thinner than in the bottom half. Measured large melt rate under ridged ice (top left) is consistent with the SHEBA experiment that the deformed ice showed a larger bottom melt rate than undeformed ice (Perovich et al., 2003). Melted thickness distribution plot shows a central peak range (0.14–0.19 m), with a mean of 0.18 m (±0.04 m), minimum of 0.10 m, and maximum of 0.35 m (Fig. 10), i.e., a mean thinning of about 2 cm day^{-1} for the work zone 2 area, corresponding to a latent heat flux of ~ 58 W m^{-2}.

4 Discussion

4.1 The "new normal" Arctic ice cover

Compared with the cruise in 2005, taken by the Oden and Healy, HOTRAX05, there were obvious differences between 2005 and 2010, in terms of ice type, concentration, thickness, snow cover, and melt pond coverage (Perovich et al., 2009). In 2005, multi-year ice was the dominant ice type with ice concentration of 80–100 % north of 79° N; in 2010, however, the dominant ice type was first year ice, even in the 12-day ice station at 87° N, and mean ice concentration in the pack ice zone was 66 % for the northward leg and 71 % for the southward leg, even less if ice in the MIZ is included. In 2005, the mean ice thickness was ~ 150 cm from 9 August (76° N) to 10 September (88.72° N); in 2010, however, the mean ice thickness was 114 cm for the northward leg and 94 cm for the southward leg, or ~ 120 cm for the pack ice zone. In 2005, it was found no snow on sea ice up to 84.3° N (29 August 2005) and about ~ 10 cm thereafter; in the 2010, a similar decomposed granular sea ice layer (less than 10 cm) was seen throughout the ice zone, besides that several snowfall events added ~ 8 cm new snow on top of the decomposed granular sea ice layer seen from 78–87.5 ° N; those new snow was then melted away due to a rainfall event on 17 August. In 2005, the pond coverage showed a clear latitudinal decrease with a mean of 35 %; in 2010, similar latitudinal trend was also shown in the pack ice zones, while the latitudinal trend is clearer in the southward

TCD
6, 1963–2004, 2012

leg than that in the northward leg, and the mean pond coverage was 25 % for the entire period.

Overall, after the record low of 2007 summer minimum ice extent in the Arctic ocean (Comiso et al., 2008; Simmonds and Keay, 2009), the ice situation in the Arctic Pacific Sector seems to have continued this different regime, i.e., a "new normal" ice cover. As compared with the 2005, the end of summer 2010 was first-year ice dominant (vs. the multiyear ice dominant), 70 % or less in ice concentration (vs. 90 %), 94–114 cm ice thickness (vs. 150 cm), no snow cover south of 78° N and 8 cm mean snow depth thereafter due to new snowfall events, and melted away, after 17 August (vs. no snow cover south 84.3° N or ~ 10 cm snow depth thereafter, after 29 August), and with pond coverage of 25 % (vs. 35 %). This change indicates the continuation of ice thinning, less concentration, and younger ice after the 2007 shift. It is not clear why the pond coverage seems to decrease as compared with the 2005 data, although one possible reason might be related to the multiyear ice dominant in 2005 that is thicker and not easy to broken into small pieces, reducing the pond coverage. The 2005 cruise was also a month later in timing and weather conditions may have played a role on surface melting in the two years.

4.2 The increased bottom melt rate

The average 2 cm day^{-1} melting rate, primarily bottom melting, during the 12-day ice station, is larger than the average ~ 0.8 cm day^{-1} during the similar period (early to middle August) of SHEBA experiments in 1998, even at lower latitudes (70–80° N) (Perovich et al., 2003). The average bottom melt in the 1998 melt season of SHEBA experiment was 62 cm, which was more than twice the amount from previous reports of 1957–1994 (Perovich et al., 2003; Eicken, 2004). This might suggest that significant change happened in the Arctic sea ice since before 1998 and is now even larger since 2007, the record low ice extent, due to warming temperature, specifically, the increased solar heating to the upper ocean that is the primary reason for the bottom melt (Perovich et al., 2008). The 12-day ice station (from 7–19 August), started at

TCD
6, 1963–2004, 2012

86.92° N/178.88° W and drifted a total of 181 km, at a rate of $0.17 \pm 0.08\,m\,s^{-1}$, was on an ice floe over 100 km^2 in size and ~ 1.8 m in mean thickness. Figure 11 shows the floe drift track and drift speed along the track during the 12-day station period, indicating a clear inertial oscillation, due to the inertial forcing (~ 12 h). The drift speed shown here is larger than long-term satellite records of 1992–2009, with mean maximum $0.12\,m\,s^{-1}$ in October (Spreen et al., 2011). Rampal et al. (2009) showed some accelerations in drift speed in recent years. Drift speed is a proxy for turbulent mixing (Perovich et al., 2003) and increased drift speed probably also played a major role for the increased bottom melt rate. Lei et al. (2012) reported drift speed in the 12-day ice station can explain 62.3 % of equivalent latent heat flux for bottom melt.

4.3 AMSR-E for mapping MIZ

In this study, based on visual observations (Fig. 4), we define the marginal ice zone (MIZ) as the ice zone with distinct difference in ice concentration and floe size from the pack ice zone. A MIZ was not clearly seen in the 2005 (or only a very narrow MIZ) based on the HOTRAX05 expedition. The MIZ in 2010, however, was clearly mapped by both the visual observation and the AMSR-E ice concentration, and extended 71.5–75° N (~ 350 km) for the northward leg (from 25–30 July) and 75.5–80° N (~ 450 km) for the southward leg (from 25–28 August). The results clearly indicate the daily AMSR-E ice concentration data could be used to map the MIZ and its change. Figure 12 show selective daily AMSR-E ice concentrations for the period from 25 July–20 September 2010 along the same northward and southward legs of the cruise. Table 2 summarizes the latitudinal extents and width of the MIZ in each day. Along the northward leg, the latitudinal extent of the MIZ was 270 km or less and minimum ice edge reached 79.1° N on 19 September. Along the southward leg, the latitudinal extent of the MIZ was more complicated with the maximum width of 500 km on 28 August; from 30 August to 20 September, there was about 100–200 km scattered ice south of the 100–200 km no ice zone before reaching the edge of the pack ice and that the minimum ice edge

TCD
6, 1963–2004, 2012

reached 77.1° N on 15 September (Table 2). The concept of passive microwave ice concentration to map the MIZ will be further examined in future cruises when similar data will be collected.

Two processes are giving a larger and more extensive MIZ, a particularly noteworthy charactistic and difference in the "new normal" Arctic compared to pre 2007. While melt pond area seems to be reduced, this could result from drainage into the leads in the lower concentration, and smaller floe sizes that are characteristic of the ice in the MIZ. The smaller floe sizes, unlike those seen in other areas, e.g. Antarctic sea ice zone, may not result from wave and swell action, but instead from floe fragmentation as melt ponds have larger connections and relative sizes than previously. These more extensive melt ponds result from an increase due to the transition from multiyear to first year ice (Itoh et al., 2011). Smaller floe sizes also transition to increased lateral melt (Steele, 1992), which feeds back to lower concentration, and further thins the ice through increased absorption of solar radiation. Once the floes are small however, they can drain into leads more easily and may account for the apparent reduction in melt pond area.

5 Summary and conclusions

This paper presents results from ship-based and visual observations of ice concentration, ice thickness, snow thickness, floe size, and melt pond coverage half hourly, over the Arctic Pacific sector during the CHINARE-2010, primarily during the period of 21 July to 28 August. In the northward leg, the highest ice concentration zone (pack ice zone) started from ~ 75° N (29 July), with ice concentration of 60–90 % (mean ~66 %), ice thickness of 1–2 m (mean ~ 1.2 m), melt ponds of 10–50 % (mean ~ 23 %) of the ice cover, ridged ice of 10–30 % of the ice cover, and floe size of 100's m to kms. There were two large and several small snowfall events, and one rainfall event in the period (29 July to 17 August). In the southward leg, the largest sea ice concentration zone (pack ice zone) was in the area between 88° N to 80° N (from 20–25 August). In this

TCD
6, 1963–2004, 2012

area, the ice concentration varied from 60–100 % (mean ~ 71 %), melt pond coverage varied from 20–50 % (mean ~ 33 %) of the ice cover, ridged ice varied from 10–30 % of the ice cover, and floe size was dominated by 10's km to several km's in one or two dimensions. The overall ice thickness decreased southwards from 1.8–2 m to 0.6–1 m. In the area from ~ 85° N to 83.5° N, we saw dirty ice (brownish, rich hills and valleys), varying from 10–20 % of the ice area. Similar dirty ice was only seen 72° N–75° N in the northward leg (24–29 July), within the MIZ.

Besides the ice concentration difference, there are clear differences in ice thickness, ice type, floe size, and pond coverage between the MIZ and the pack ice zone. We summarize those parameters in the MIZ of the 2010 cruise as the following. The ice thickness of the highest concentration was 100 cm in late July (northward leg) and thinned to less than 50 cm in later August (southward leg); ice type was either thick first year ice or multiyear ice, with good portion of dirty ice (animal associated) for the northward leg, while it seems the same type of ice but much thinner in the southward leg; floe size was typically 2–100 m; melt pond coverage was 16 % for the northward leg and 10 % for the southward leg.

We also compared visually observed ice concentration and thickness (half-hourly) with the high temporal resolution data from automated video-camera recording and hanging EM31 measurements, respectively. Although there are large differences in terms of sampling frequency and area between the half-hourly visual observations and the 10 s video camera recording (EISCam) and the one second EM31 thickness data, the information provided from different means show some match to a degree. Both EISCam and EM31 provide detailed information of sea ice situation, while the visual observations provide only shots half-hourly, with a broad view (1km radius of circle area) and incorporate observer variability and experience. The orthorectified EISCam images provide a permanent record of ice concentration and melt pond and can also be used to derive detailed pond size distributions, floe sizes, and lead widths. In addition, both the EISCam and EM31 provide systematic datasets better suited to quantitative

TCD
6, 1963–2004, 2012

analyses as compared with the visual observations with possible bias from different observers and from different cruises leading to uncertainty in their identification of change.

An 8-profile grid of ice thickness measurements (four repeats) was conducted in the heart of the Central Arctic Ocean and an average 2 cm day^{-1} melting rate, primarily bottom melting, was found. The design of such a grid enables us to do a sea ice thickness study, by producing an ice thickness map of a sizable area and to study the changes from time to time using repeated measurements. This dataset would be even more valuable for calibration and/or validation purposes, if simultaneous airborne or satellite measurements of ice thickness can be made. The Cryosat2 was launched in April 2010 and should have overlapped with the 7–19 August 2010 when the grid measurements were conducted. It is our intention to use the field data for such a validation of Cryosat2's sea ice freeboard and thickness data when it will be available.

The combined information from all those data provide a broad view of sea ice cover for its spatial and temporal variations over the Pacific Arctic sector for the study period. This invaluable dataset can be used for comparison with previous data or as a benchmark for future change.

Acknowledgements. The study was partially supported by the NASA grant (#NNX08AQ87G), the Chinese NSF grant (#40930848), and the National High Technology Research and Development Program of China (#2010AA09Z103). Travel expenses for H. Xie for the cruise were covered by NOAA's Climate Research/Sea Ice Outlook Program. We sincerely acknowledge the support from the Chinese Arctic and Antarctic Administration, the Chinese Arctic Expedition Team-2010, the other persons of sea ice team of the cruise, and the two graduate students, Wentao Xia and Yunbo Bi at the Laboratory for Remote Sensing and Geoinformatics in UTSA who helped process some data.

References

Comiso, J. and Nishio, F.: Trends in the sea ice cover using enhanced and compatible AMSR-E SSM/I and SMMR Data, J. Geophys. Res., 113, C02S07, doi:10.1029/2007JC004257, 2008.

TCD
6, 1963–2004, 2012

Darby, D. A., Myers, W. B., Jakobsson, M., and Rigor, I.: Modern dirty sea ice characteristics and sources: The role of anchor ice, J. Geophys. Res., 116, C09008, doi:10.1029/2010JC006675, 2011.

Eicken, H., Grenfell, T. C., Perovich, D. K., Richter-Menge, J. A., and Frey, K.: Hydraulic controls of summer Arctic pack ice albedo, J. Geophys. Res., 109, C08007, doi:10.1029/2003JC001989, 2004.

Eicken, H., Gradinger, R., Gaylord, A., Mahoney, A., Rigor, I., and Melling, H.: Sediment transport by sea ice in the Chukchi and Beaufort Seas: increasing importance due to changing ice condtions?, Deep-Sea Res. Pt. II, 52, 3281–3302, 2005.

Giles, K. A., Laxon, S. W., Wingham, D. J., Wallis, D. W., Krabill, W. B., Leuschen, C. J., McAdoo, D., Manizade, S. S., and Raney, R. K.: Combined airborne laser and radar altimeter measurements over the Fram Strait in May 2002, Remote Sens. Environ., 111, 182–194, 2007.

Giles, K. A., Laxon,S. W., and Ridout, A. L.: Circumpolar thinning of Arctic sea ice following the 2007 record ice extent minimum, Geophys. Res. Lett., 35, L22502, doi:10.1029/2008GL035710, 2008.

Hass, C. and Druckenmiller, M.: Ice thickness and roughness measurements, in: Field Techniques for Sea Ice Research, edited by: Eicken et al., University of Alaska Press, 565 pp., 2009.

Haas, C., Pfaffling, A., Hendricks, S., Rabenstein, L., Etienne, J. L., and Rigor, I.: Reduced ice thickness in Arctic Transpolar Drift favors rapid ice retreat, Geophys. Res. Lett., 35, L17501, doi:10.1029/2008GL034457, 2008.

Itoh, M., Inoue, J., Shimada, K., Zimmermann, S., Kikuchi, T., Hutchings, J., McLaughlin, F., and Carmack, E.: Acceleration of sea-ice metling due to transmission of solar radiation through ponded ice area in the Arctic Ocean: results of in situ observations from icebreakers in 2006 and 2007, Ann Glaciol., 52, 249–260, 2011.

Kempema, E. W., Reimnitz, E., and Barnes, P. W.: Sea ice sediment entrainment and rafting in the Arctic, J. Sediment. Petrol., 59, 308–318, doi:10.1306/212F8F80-2B24-11D7-8648000102C1865D, 1989.

Kwok, R. and Rothrock, D. A.: Decline in Arctic sea ice thickness from submarine and ICESat records: 1958–2008, Geophys. Res. Lett., 36, L15501, doi:10.1029/2009GL039035, 2009.

TCD
6, 1963–2004, 2012

Lei, R., Zhang, Z., Matero I., Cheng, B., Li, Q., and Huang, W.: Reflection and transmission of irradiance by snow and sea ice in the central Arctic Ocean in summer 2010, Polar Res., 31, 17325, doi:10.3402/polar.v31i0.17325, 2010.
Leppäranta, M.: The Drift of Sea Ice, ISBN 3-540-40881-9, Springer-Praxis Books in Geophysical Sciences, Chichester, UK, 266 pp., 2005.
Lu, P., Li, Z., Cheng, B., Lei, R., and Zhang, R.: Sea ice surface features in Arctic summer 2008: Aerial observations, Remote Sens. Environ., 114, 693–699, doi:10.1016/j.rse.2009.11.009, 2010.
Maslanik, J. A., Fowler, C., Stroeve, J., Drobot, S., Zwally, J., Yi, D., and Emery, W.: A younger, thinner Arctic ice cover: increased potential for rapid, extensive sea-ice loss, Geophys. Res. Lett., 34, L24501, doi:10.1029/2007GL032043, 2007.
Nghiem, S. V., Rigor, I. G., Perovich, D. K., Clemente-Colon, P., Weatherly, J. W., and Neumann, G.: Rapid reduction of Arctic perennial sea ice, Geophys. Res. Lett., 34, L19504, doi:10.1029/2007GL031138, 2007.
Perovich, D. K.: The changing Arctic sea ice cover, Oceanography, 24, 162–173, doi:10.5670/oceanog.2011.68, 2011.
Perovich, D. K., Grenfell, T. C., Light, B., and Hobbs, P. V.: Seasonal evolution of the albedo of multiyear Arctic sea ice, J. Geophys. Res., 107, 8044, doi:10.1029/2000JC000438, 2002.
Perovich, D. K., Grenfell, T. C., Richter-Menge, J. A., Light, B., Tucker III, W. B., and Eicken, H.: Thin and thinner: sea ice mass balance measurements during SHEBA, J. Geophys. Res., 108, 8050, doi:10.1029/2001JC001079, 2003.
Perovich, D. K., Richter-Menge, J. A., Jones, K. F., and Light, B. Sunlight, water, and ice: extreme Arctic sea ice melt during the summer of 2007, Geophys. Res. Lett., 35, L11501, doi:10.1029/2008GL034007, 2008.
Perovich, D. K., Grenfell, T. C., Light, B., Elder, B. C., Harbeck, J., Polashenski, C., Tucker III, W. B., and Stelmach, C.: Transpolar observations of the morphological properties of Arctic sea ice, J. Geophys. Res., 114, C00A04, doi:10.1029/2008JC004892, 2009.
Rampal, P., Weiss, J., and Marsan, D.: Positive trend in the mean speed and deformation rate of Arctic sea ice, 1979–2007, J. Geophys. Res., 114, C05013, doi:10.1029/2008JC005066, 2009.
Serreze, M. C., Barrett, A. P., Slater, A. G., Steele, M., Zhang, J., and Trenberth, K. E.: The large-scale energy budget of the Arctic, J. Geophys. Res., 112, D11122, doi:10.1029/2006JD008230, 2007.

TCD
6, 1963–2004, 2012

Simmonds, I. and Keay, K.: Extraordinary September Arctic sea ice reductions and their relationships with storm behavior over 1979–2008, Geophys. Res. Lett., 36, L19715, doi:10.1029/2009GL039810, 2009.
Spreen, G., Kwok, R., and Menemenlis, D.: Trends in Arctic sea ice drift and role of wind forcing: 1992–2009, Geophys. Res. Lett., 38, L19501, doi:10.1029/2011GL048970, 2011.
Squire, V. A.: Of ocean waves and sea-ice revisited, Cold Reg. Sci. Technol., 49, 110–133, 2007.
Steele, M.: Sea ice melting and floe geometry in a simple ice-ocean model, J. Geophys. Res., 94, 17729–17738, 1992.
Stroeve, J., Holl, M., Meier, W., Scambos, T., and Serreze, M.: Arctic sea ice decline: faster than forecast, Geophys. Res. Lett., 34, L09501, doi:10.1029/2007GL029703, 2007.
Weissling, B., Lewis, M. J., and Ackley, S. F.: Sea ice thickness and mass at Ice Station Belgica, Bellingshausen Sea, Antarctica, Deep-Sea Res. Pt. II, 58, 1112–1124, doi:10.1016/j.dsr2.2010.10.032, 2011.
Weissling, B. P., Xie, H., and Murray, K.: Evaluation of NRCS curve number and MODIS time series proxies for antecedent moisture condition, Civ. Eng. Environ. Syst., 26, 85–101, doi:10.1080/10286600802005356, 2009.
Worby, A. P. and Allison, I.: A technique for making ship-based observations of Antarctic sea ice thickness and characteristics, Part I: Observational technique and results, Antarctic CRC Research Report, 14, 1–23, 1999.
Worby, A. P., Geiger, C., Paget, M., Van Woert, M., Ackley, S., and DeLiberty, T.: Thickness distribution of Antarctic Sea Ice, J. Geophys. Res., 113, C05S92, doi:10.1029/2007JC004254, 2008.
Wang, J., Guo, J., Wang, H., Sun, B., and Tian, G.: Data analysis of shipborne EM31-ice measurmening in China's fourth Arctic scientific expedition, Chinese Journal of Polar Research, 24, 47–52, doi:10.3724/SP.J.1084.2012.0000, 2012.
Xie, H., Ackley, S. F., Yi, D., Zwally, H. J., Wagner, P., Weissling, B., Lewis, M., and Ye, K.: Sea ice thickness distribution of the Bellingshausen Sea from surface measurements and ICESat altimetry, Deep-Sea Res. Pt. II, 58, 1039–1051, doi:10.1016/j.dsr2.2010.10.038, 2011.
Zwally, H. J., Schutz, B., Abdalati, W., Abshire, J., Bentley, C., Brenner, A., Bufton, J., Dezio, J., Hancock, D., Harding, D., Herring, T., Minster, B., Quinn, K., Palm, S., Spinhirne, J., and Thomas, R.: ICESat's laser measurements of polar ice, atmosphere, ocean, and land, J. Geodyn., 34, 405–445, 2002.

TCD
6, 1963–2004, 2012

Zwally, H. J., Yi, D., Kwok, R., and Zhao, Y.: ICESat measurements of sea ice freeboard and estimates of sea ice thickness in the Weddell Sea, J. Geophys. Res., 113, C02S15, doi:10.1029/2007JC004284, 2008.

TCD
6, 1963–2004, 2012

Table 1. EM 31 profiles and sampling points in each station.

Ice stations	Profiles	Points	Comments
IS-1 (27 Jul)	1	88	Short profile (1 m interval)
IS-2 (30 Jul)	4	161	Short profiles (1 m interval)
IS-3 (1 Aug)	3	167	Short profiles (1 m interval)
IS-4 (3 Aug)	5	118	Short profiles around two melting ponds (1 m interval)
IS-5 (5 Aug)	4 1	226 230	Short profiles (1 m interval) One circle covering the entire floe (continuous mode)
LIS (7–19 Aug)	8 (work zone 2) 2 (work zone 3)	640 (160 × 4) 390 (130 × 3)	Four repeats for the 8 profiles (5 m interval) Three repeats for the 2 profiles (2.5 m interval)
IS-6 (20 Aug)	1	239	One circle covering the entire floe (continuous mode)
IS-7 (23 Aug)	1	138	One circle covering the entire work zone (1 m interval)
IS-8 (24 Aug)	1	409	One circle covering the entire floe (continuous mode)
Total	31	2957	

TCD
6, 1963–2004, 2012

Table 2. Latitudinal extents (and width in km) of the marginal ice zone (MIZ) along the northward and southward legs on selected days (MMDD) based on AMSR-E ice concentration products.

	0725	0729	0820	0825	0828	0830	0905	0910	0915	0919
Northward leg	71.5–74.8° (270)	72.8–75.1° (230)	75.6–77.3° (170)	75.6–78.0° (240)		75.8–78.0° (220)	78.2–80.9° (270)	78.6–81.1° (250)	78.7–78.9° (20)	79.1–79.6° (50)
Southward leg			xxx–77.5°	xxx–80.0°	75.5–80.5° (500)	75.5–79.5° (400*)	75.5–79.5° (400*)	75.7–80.6° (490*)	77.1–80.4° (330*)	76.9–80.6° (370*)

xxx denotes MIZ beyond the last ship-based observation on 28 August;
* denotes there is a 200 km or less region of no ice zone between the packed ice edge and scattered ice zone.

TCD
6, 1963–2004, 2012

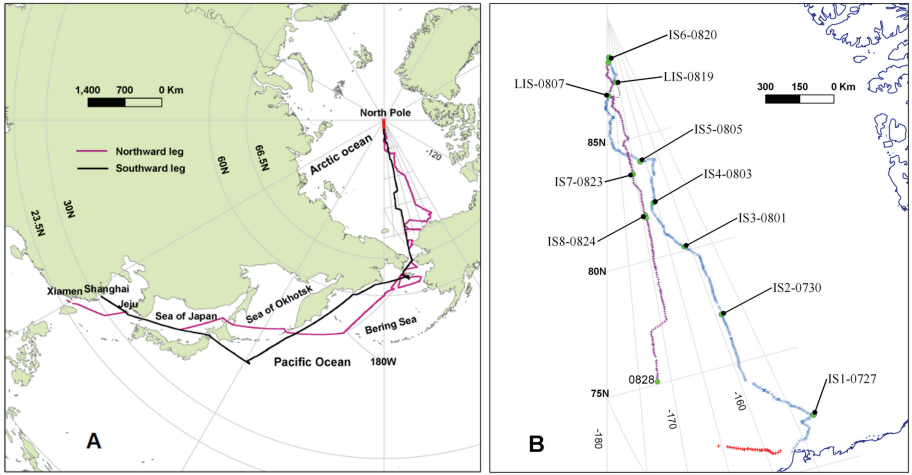

Fig. 1. (A) The ship tracks from Xiamen, China (1 July) to Central Arctic and back to Shanghai, China (20 September), 2010; **(B)** The ship-based half-hourly visual observations of sea ice (red: westward; blue: northward; magenta: southward), ice station (IS) locations (green dots), number and date (MMDD) conducted; LIS denotes the 12-day ice station from 7 to 19 August (black line). The green dot (0828, 28 August) was the last ice observation where the ship left the ice zone.

TCD
6, 1963–2004, 2012

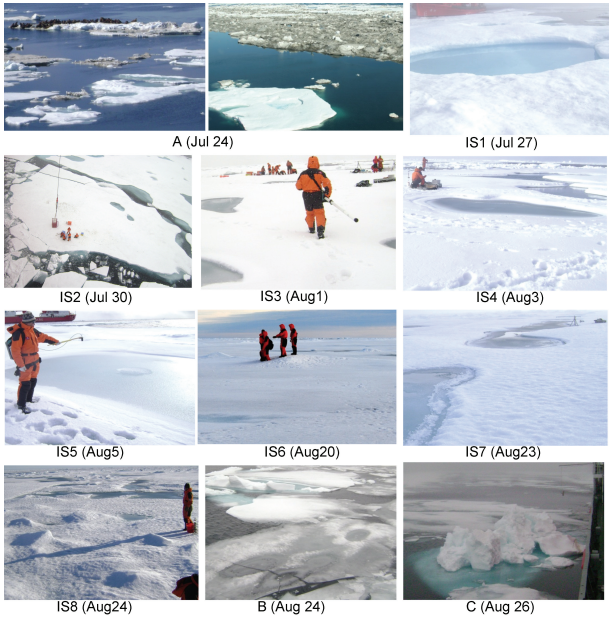

Fig. 2. Photos of typical snow and ice taken from the ship or on the eight short-term ice stations (IS1 to IS8) from the 2010 cruise. **(A)** dirty ice in the marginal ice zone, left photo: hundreds of walruses were seen over dirty ice; right photo: a floe size of 500 m dirty ice with rough surface of up to 2 m in thickness; **(IS1)** loose granular sea ice layer of depth 2–8 cm, blue color pond, with Huanghe (red boat) on top left; **(IS2)** loose granular sea ice layer of depth 2–8 cm, **(IS3)** new snow of 5–6 cm on top, a mean depth of 13 cm with a loose granular sea ice layer below new snow; **(IS4)** new snow on top, a mean depth of 15 cm with loose granular sea ice layer below the new snow; **(IS5)** new snow on top, a mean depth of 15 cm; **(IS6)** refrozen granular sea ice layer snow (firn-like), mean depth of 10 cm; **(IS7)** refrozen granular sea ice layer I (firn-like), mean depth of 10 cm; **(IS8)** refrozen granular sea ice layer (firn-like), a mean depth of 10 cm; **(B)** thin new ice and old thicker ice with blue melt ponds; **(C)** floeberg of 10 m in diameter and over 4 m above the sea surface, hit by the hanging EM31 (up right corner).

TCD
6, 1963–2004, 2012

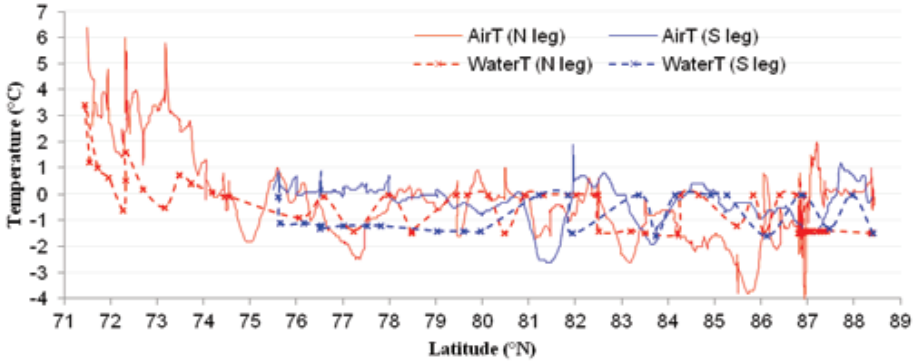

Fig. 3. Ship-based air (solid lines) and water (dashed lines) temperatures for northward leg (red, 25 July–20 August) and southward leg (blue, 20–28 August) during the CHINARE-2010. The air temperature was continuous measurements and water temperature was interupted once the ship was moving in the ice. Detailed timing and locations of ice stations should refer to Figs. 1 and 4a.

TCD
6, 1963–2004, 2012

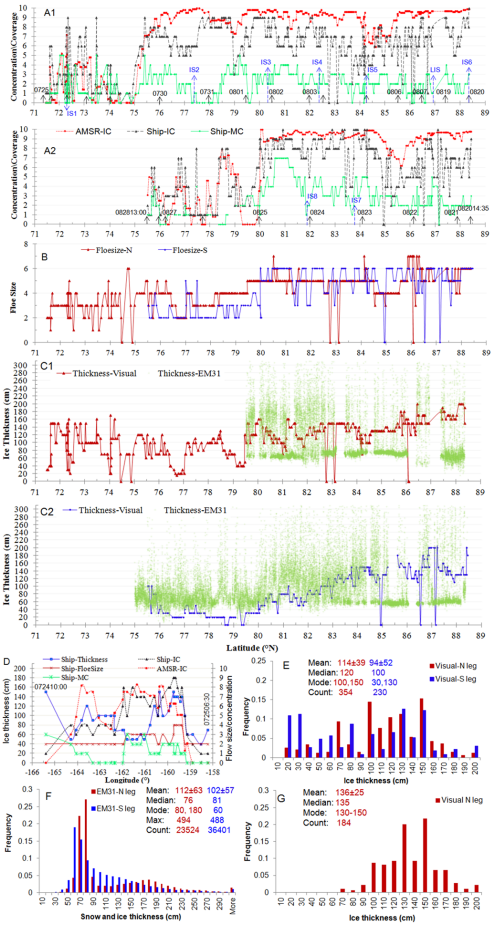

Fig. 4. (Caption on next page.)

TCD
6, 1963–2004, 2012

Fig. 4. Ship-based visual observations of sea ice thickness, floe size, melt pond coverage (MC), and concentration (IC), and AMSR-E ice concentration during the CHINARE-2010, from 24 July, 10:00 UTC to 25 July, 06:30 UTC (westward leg, **D**), 25 July–20 August (northward leg, **A1**, **B**, **C1**), and 20–28 August (southward leg, **A2**, **B**, **C2**), with ice thickness distributions shown in **(E)**. The EM31-derived snow and ice thickness are also included (**C1** and **C2**) for comparison purpose, with corresponding thickness distributions also included (**F** for EM31 and **G** for corresponding viusal observations in the northward leg). Location of ice stations (IS1 to IS8) and date (with time) are also marked in **(A1)** and **(A2)**; Floe size code: 1 (< 2 m), 2 (2–20 m), 3 (20–100 m), 4 (100–500 m), 5 (500–2000 m), 6 (2–10 km), and 7 (>10 km). Ship traveled westward in the Marginal ice zone of 280 km or ~ 40 km per longitude degree **(D)**. It is about 100 km per latitude degree **(A, B, C)**.

TCD
6, 1963–2004, 2012

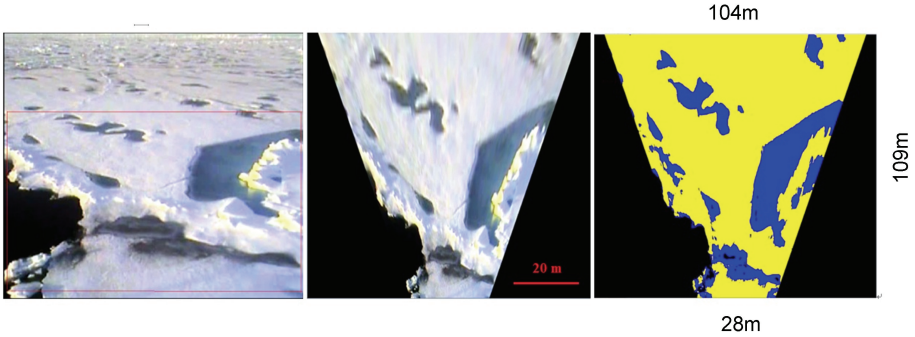

Fig. 5. An EISCam video image (03:20:50 UTC, 23 August) of oblique view with red outlined area to be good quality for orthorectification (left panel), orthorectified image (middle panel) and threhold classification results (right panel), with black for open water (9 %), blue for melt pond (27 %), and yellow for ice (64 %). Threhold values used for this image are 0–94 for water, 95–160 for melt pond, and 161–255 for ice.

TCD
6, 1963–2004, 2012

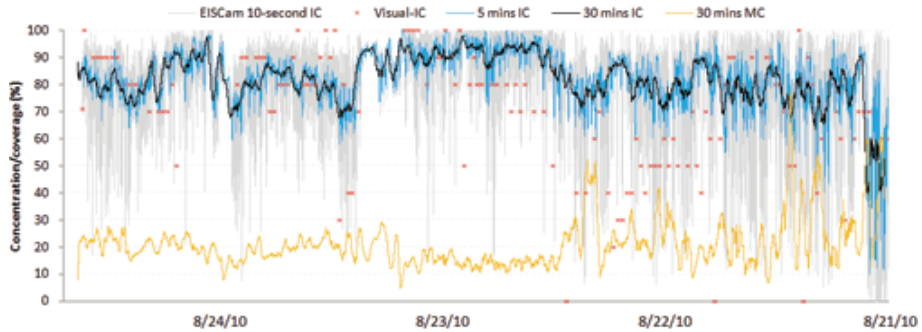

Fig. 6. EISCam video image-derived ice concentration (IC) at the original 10 s, 5 min and 30 min moving average scales, and melt pond coverage (MC) at the 30 min moving average scale, with the corresponding ship-based visual observed IC (once per 30 min) from the 21 August 2010 (00:18 UTC) to 24 August 2010 (15:10 UTC), the first half of the southward leg.

TCD
6, 1963–2004, 2012

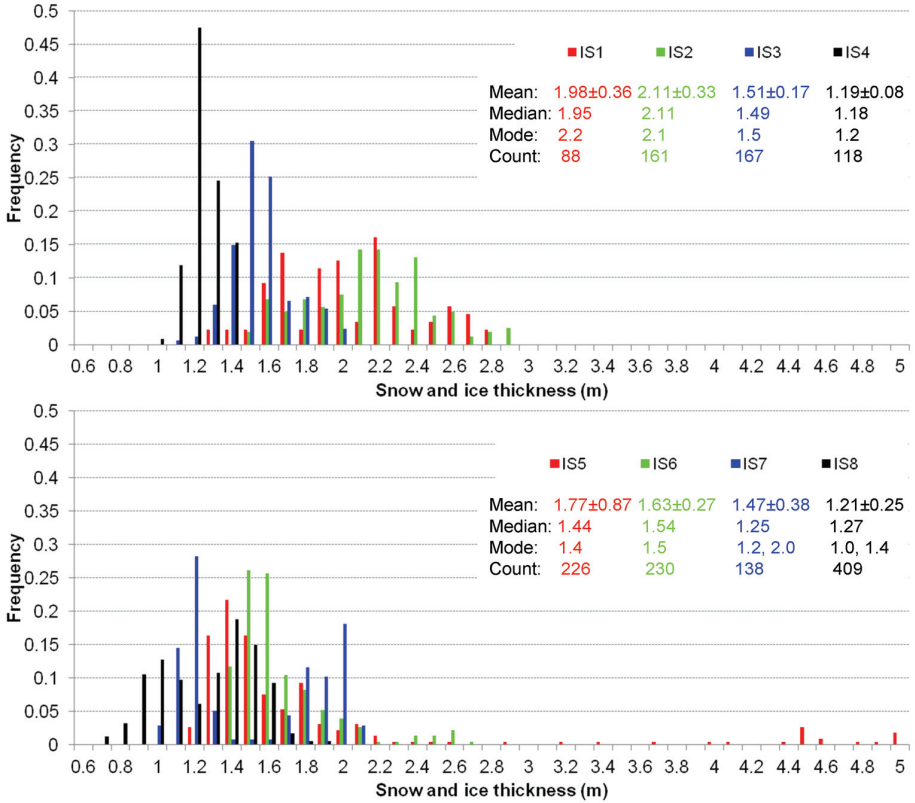

Fig. 7. EM31-measured snow and ice thickness distribution and statistics from the 8 short-term ice stations of the 2010 cruise.

TCD
6, 1963–2004, 2012

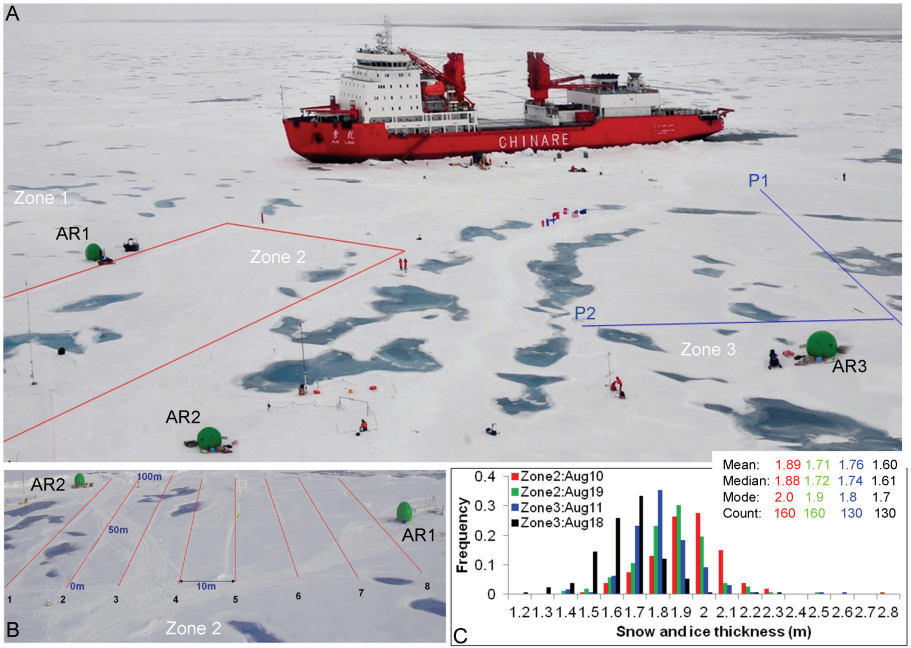

Fig. 8. The 12-day ice station (7–19 August) over the ice floe of more than 10 km × 10 km, mainly thick first year ice **(A)**, with R/V Xuelong in the back, and three work zones and three apple rooms (AR) marked; A grid of 8 profiles (100 m long and 10 m apart) in zone 2 **(B)** and two profiles (200 m for P1 and 125 m for P2) in zone 3 used for repeated sea ice thickness measurements using the EM31; Sea ice thickness distribution and basic statistics from the first and last measurements over zone2 and zone3 **(C)**. A crack (whiter or higher albedo than surrounding) along and crossing the line 5 in work zone 2 is clearly seen **(B)**.

TCD
6, 1963–2004, 2012

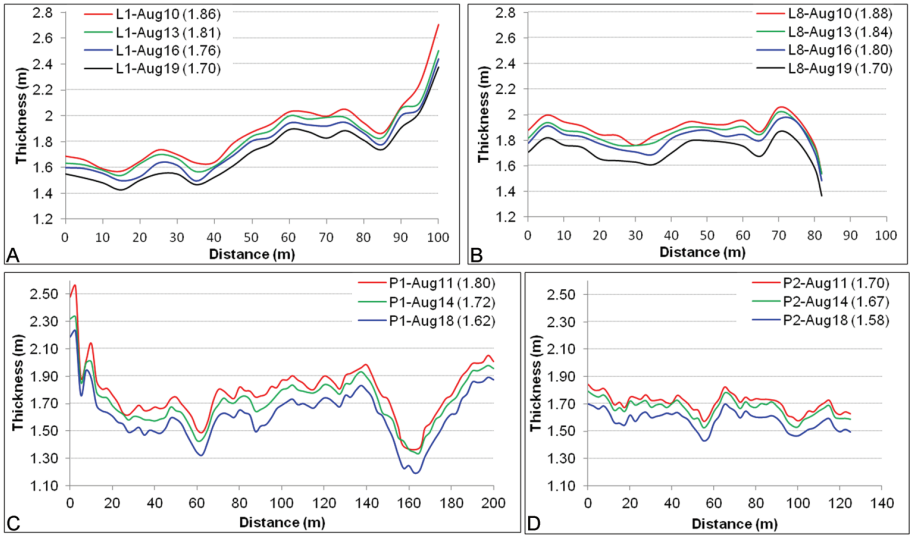

Fig. 9. Examples of repeated EM31 snow and ice thickness measurements: **(A)** and **(B)** respectively for profile line 1 and line 8 in work zone 2; **(C)** and **(D)** respectively for profile P1 and P2 in work zone 3. Number in the brackets is the mean thickness of the profile measured in that day. The start points (or 0 m distance) of profiles in Zone 2 were marked in Fig. 8b; the start point of P2 was the intersection point of P2 and P1, while the start point of P1 was out of the Fig. 8a, to the lower right corner.

TCD
6, 1963–2004, 2012

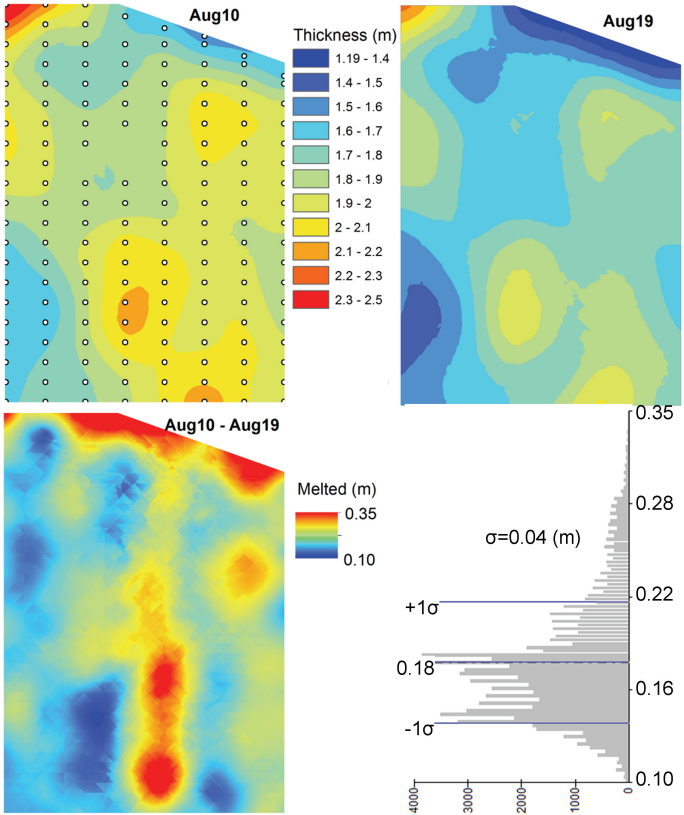

Fig. 10. Snow and ice thickness maps of Aug10, Aug19, difference map (or melted ice) between Aug10 and Aug19, and frequency distrubution of the difference map (mean 0.18 m and standard deviation of 0.04 m). The small circles on the Aug10 map show the locations of individual EM31 measurements (5 m apart along the profile and 10 m apart between profiles).

TCD
6, 1963–2004, 2012

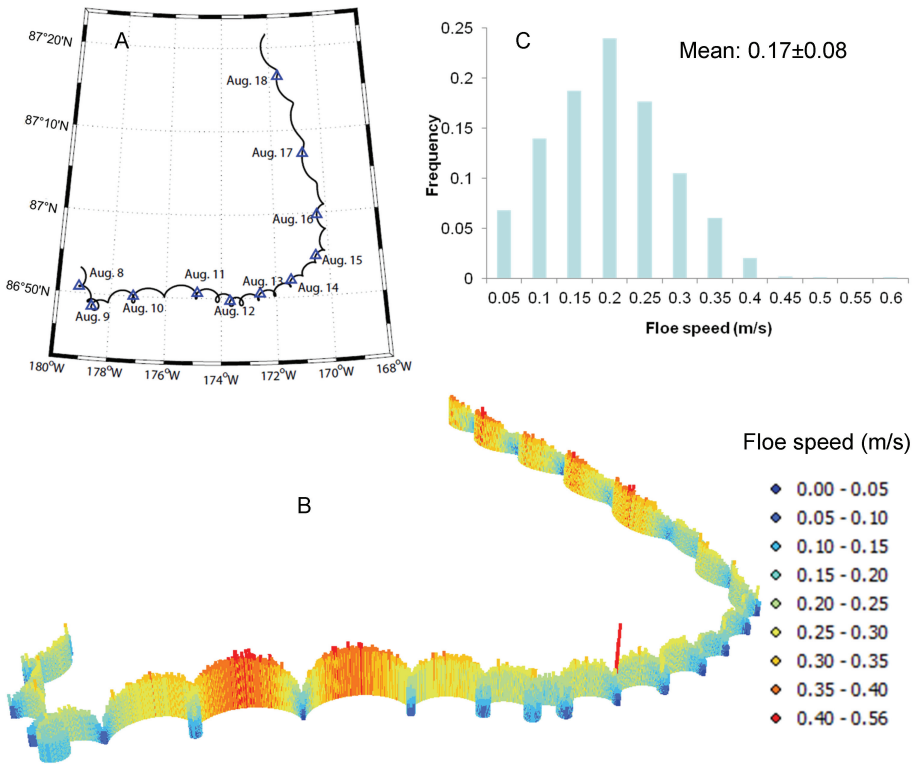

Fig. 11. Floe drift track **(A)**, floe speed in 3-dimensional view **(B)**, and floe speed distribution **(C)** during the 12-day ice station.

TCD
6, 1963–2004, 2012

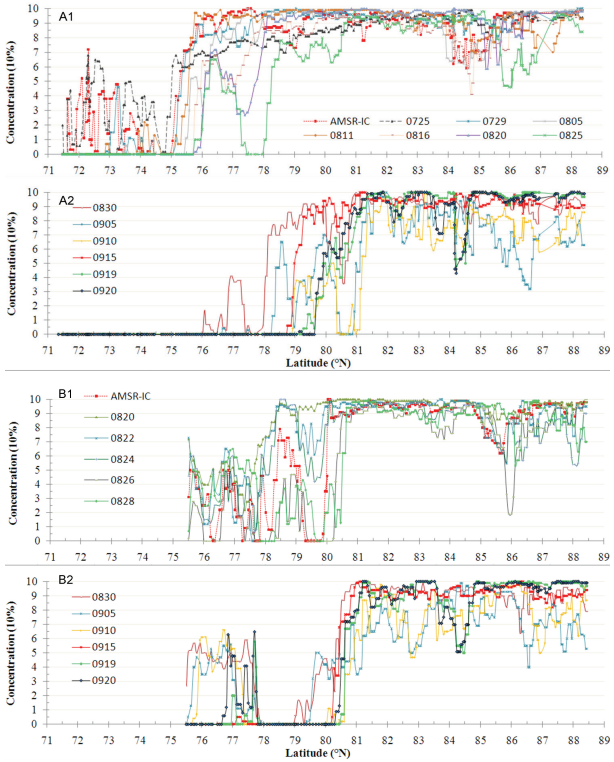

Fig. 12. Daily AMSR-E ice concentrations for the northward **(A)** and southward **(B)** legs. The AMSR-IC curves are from the Fig. 4a, respectively for the time period 25 July to 20 August (northward leg) and 20 to 28 August (southward leg).

TCD
6, 1963–2004, 2012